Formation of non-uniform fibre distribution and its effect on the flexural performance of pultruded GFRP box beams

Songming Qi [a,*], Omar Alajarmeh [a], Mohammad Alhawamdeh [b], Tristan Shelley [a], Peter Schubel [a], Kendric Rendle-Short [c], Xuesen Zeng [a]

[a] *University of Southern Queensland, Centre for Future Materials, Toowoomba Queensland 4350, Australia*
[b] *Tafila Technical University, Department of Civil Engineering, Tafila 66110, Jordan*
[c] *Wagners Composite Fibre Technologies, Wellcamp Queensland 4350, Australia*

ARTICLE INFO

ABSTRACT

This study investigates the effect of non-uniform fibre distribution (NUFD) as a defect in the pull-winding manufacturing process on the mechanical properties of pultruded glass fibre-reinforced polymer (GFRP) box section profiles. These profiles exhibit balanced mechanical properties but are susceptible to NUFD during production, negatively affecting local buckling capacity. Experimental and numerical analyses were conducted on pultruded GFRP profiles manufactured under three winding tension configurations, resulting in a 5% variance in load capacity during bending. Results show that corner NUFD influences local buckling capacity more than flange NUFD. Specifically, corner NUFD decreases load capacity by up to 20%, while flange NUFD increases it by up to 3%. Conversely, the effect of NUFD location is insignificant to the failure determined by the material strength without buckling instability. Moreover, a linear relationship between the rotational restraint coefficient and corner fibre volume fraction provides insight into the impact of material imperfections on load capacity.

1. Introduction

Pultruded fibre-reinforced polymer (pFRP) profiles have gained widespread use in civil infrastructure applications due to their high strength-to-weight ratio, corrosion resistance and low maintenance requirements [1–4]. However, due to the low stiffness and anisotropic nature of pFRP, deflections and buckling instabilities are commonly observed in structures subjected to axial and flexural loading, particularly in thin-walled structures [5–7]. Local buckling, which occurs prior to material failure, is a critical factor in predicting the structural capacity of the pFRP sections [8–10].

Local buckling analysis of the pFRP profile is typically performed using the plate theory [11–13], with separate calculations for the flange and web loading capacities and considering the flexibility of the flange-web connections. Qiao et al. [14] presented an explicit formulation and elastic constraint coefficient to determine the local buckling capacity of a box section under compression loading. Kollár [15] proposed a refined equation for the constraint coefficient at the corners. It should be noted that local buckling in pFRP profiles under compression loading differs from that under bending loading, as only the top flange and partial web

buckle are under compression [16]. Liu et al. [17] investigated the contribution of the rotational stiffness at the flange-web junction to flange local buckling (FLB) under bending. They found that the fibre–matrix architecture would affect the stiffness of flange edge support. Further research is required to fully understand the impact of fibre–matrix architecture on local buckling behaviour in pFRP profiles.

Pull-winding technology, a combination of pultrusion and filament winding, is a high-volume and cost-effective production method [18,19], as shown in Fig. 1(a). This process utilises continuous-wound fibres to reinforce the transverse properties of pFRP composites [20,21]. The wound fibre increases the rotation stiffness at the corner to resist local buckling [22]. However, the wound fibres are susceptible to causing non-uniform fibre distribution (NUFD) across the cross-section of pFRP profiles. When the dry fibre preform produced in the pull-winding process passes into and through the pultrusion die, the associated compaction generates excess length in the wound fibres, leading to both in-plane and out-of-plane waviness [23]. The interaction between wavy fibres and unidirectional (UD) fibres leads to lateral shifting in the latter. As a result, the cross-section exhibits NUFD, particularly in the corner (Fig. 1(c)).

Winding tension is a critical manufacturing factor influencing the initial thickness of the fibre preform [24]. The winding tension is controlled by the yarn path with steel pins [25] (Fig. 1(b)); higher tension generates a thinner preform but also increases the resin injection pressure and pulling force. This research used three different winding tensions to manufacture profiles to obtain varying degrees of NUFD.

Various numerical modelling methods have been employed to assess the flexural performance of the GFRP box, including the Finite Element Method [17], Finite Difference Method [26], Bezier Multi-Step Method [27], and Differential Quadrature Method [28]. These methods offer valuable insights into the composite profiles' structural behaviour and mechanical response under bending conditions. The presence of NUFD in the pFRP profiles can negatively impact the structural integrity and mechanical performance. The influence of NUFD on mechanical strength is regulated in the Chinese standard GB/T 31539–2015 [29]. Zhang et al. [30] found that non-uniform fibre packing over a cross-section has a limited effect on compressive strength based on the finite element (FE) model. However, their study did not consider the specific locations of defects in full-scale profiles, including corner defects and wall defects. Feng. et al. [31] reported NUFD significantly impacts the global buckling of pFRP profiles under compression. For I-sections with a slenderness ratio (span/depth) of 70, NUFD results in a resistance reduction factor of 0.88. This reduction factor represents the ratio of the maximum compressive stress captured by the non-uniform material model to that captured by the uniform material model. However, no study was found on the effect of NUFD on the flexural performance of pFRP profiles. This research will focus on the NUFD effect on flexural behaviour.

The characterisation of non-uniform fibre-resin distribution (e.g. fibre wrinkle, fibre flip, fibre waviness and resin-rich zone) has been discussed previously, and its influence on the performance of FRP composites has been examined. Wilhelmsson et al. [32] presented a high-resolution misalignment analysis to identify the maximum fibre misalignment to predict the compressive strength of non-crimp fabrics, while Qi et al. [33] showed the effect of fibre misalignment on stress distribution using the FE method. Poulton and Sebastian [34] presented a taxonomy of mat misalignment by comparing the actual location to the idealised location using manually plotted points. Feng et al. [31] adopted the calcination test to measure the resin content in the specified locations from different FRP sections. In addition, X-ray micro-computed tomography was used to characterise the internal geometry of the resin-rich area [35]. Netzel et al. [36] quantified the wrinkling severity and material flow with an optical microscope. This research adopts an image analysis method to measure the UD fibre content along the cross-section, offering more details on the fibre distribution and facilitating a more accurate FE modelling.

In this research, box section pFRP profiles manufactured with various wound fibre tension were tested under bending to examine the effect of the NUFD on FLB experimentally and numerically. The NUFD was considered by changing the fibre volume fraction (Vf) across the section, which is more convenient than the calcination method. A numerical model was built up and verified to study the sensitivity of the buckling load towards the NUFD under four-point bending based on the predefined fibre distribution. The results demonstrated the significance of considering the material imperfection effect on the flexural load capacity.

2. Experimental program

In this research, two different sizes of box section profiles, S100 and S125, were manufactured using pull-winding technology by Wagners Composite Fibre Technology (WCFT). These profiles were made from E-glass fibres (Jushi fibres at 4800 tex) with a 2.54 g/cm^3 density, impregnated via an injection die using vinyl ester (Viapal) resin. Fig. 2 (a) shows the geometric and cross-sectional detail of the profile, and the specifications are listed in Table 1.

As shown in Fig. 1(b), the winder regulates the yarn tension through the position of the yarn path and steel pins. The wound fibre tension was measured using a digital force gauge with a resolution of 0.1 N, resulting in three values of 2.2 N, 15.3 N and 48.3 N. These three yarn tensions corresponded to low, medium and high wound fibre tensions, respectively, and were used to manufacture S125 samples with varying degrees of NUFD. The S100 samples are manufactured at medium tension.

The fibre distribution along the pultrusion direction has been previously observed to be uniform [37], and this aspect will be discussed in Section 3.3. Therefore, for material testing purposes, the selected coupons in each group were cut along the pultrusion direction. These coupons were chosen from both S125 and S100 profiles, ensuring they exhibited no noticeable fibre waviness across the cross-section, as shown in Section A-A Fig. 3(b). This absence of waviness was verified through
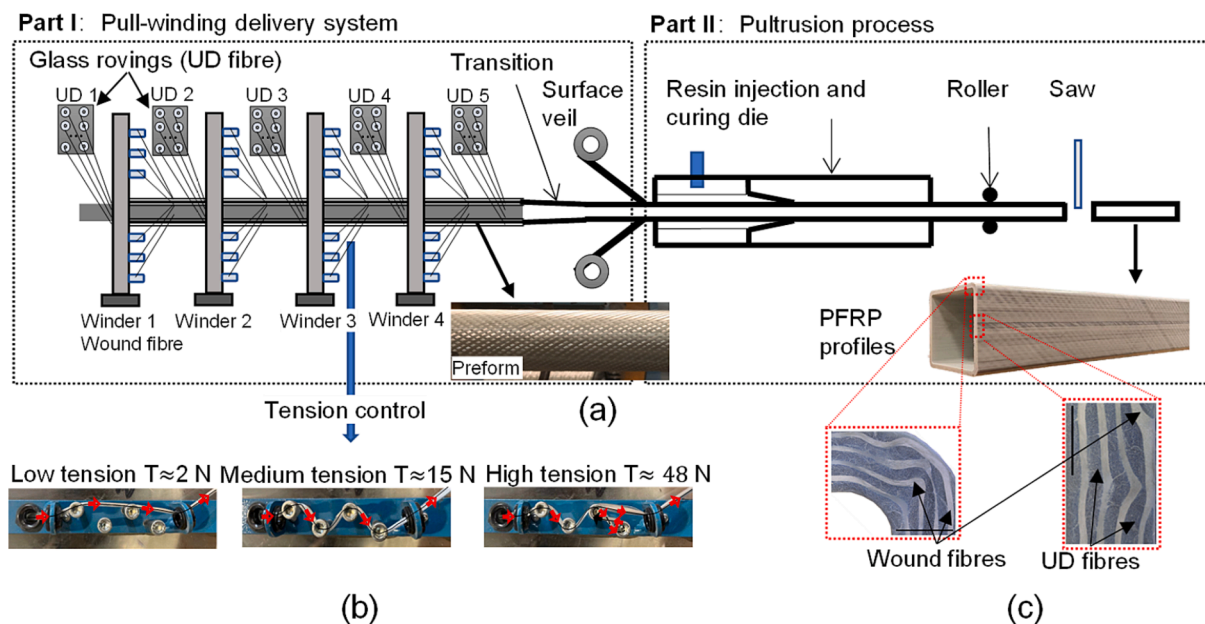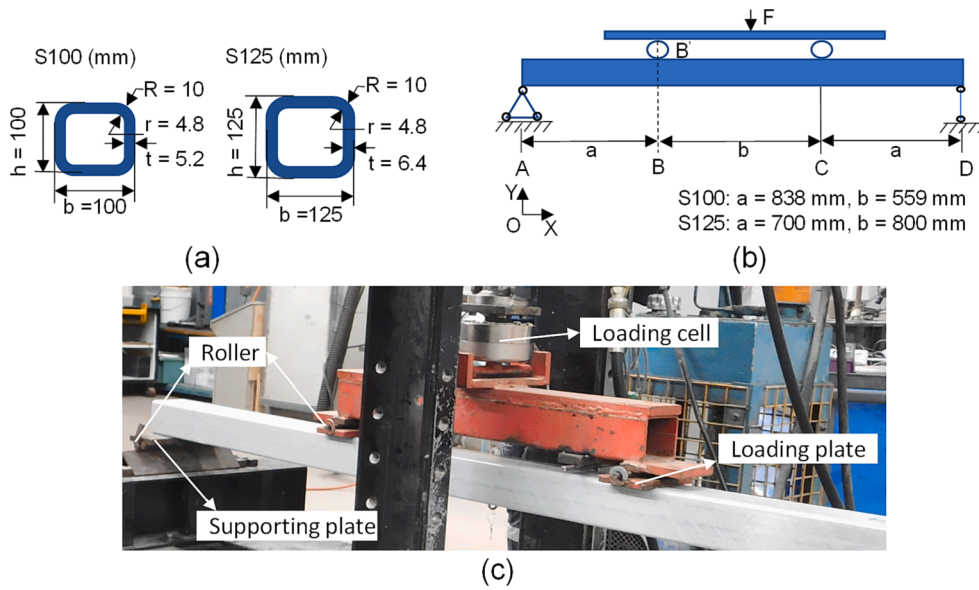

Fig. 1. Illustration of pull-winding pultrusion process and its products; (a) pull-winding technique, (b) winding tension control and (c) non-uniform fibre distribution.

Fig. 2. Flexural test setup; (a) cross-sectional dimensions of S100 and S125, (b) beams spans for four-point bending tests and (c) four-point bending test configuration.

Table 1
Layup and geometric properties of hollow pFRP profiles.

Profile label	Dimensions (mm)	Layup properties		
		Fibre content (%)	Fibre VF (%)	Stacking sequence
S100	100 × 100 × 5.2	0°: 82.2 50°: 17.8	60.5	0/+50/-50/0/-50/+50/0
S125	125 × 125 × 6.4	0°: 78.1 50°: 21.9	62.5	0/+50/0/-50/0/-50/0/+50/0

the polishing process, allowing for a thorough assessment of the fibre distribution [33]. Each group consisted of ten coupon replicates to ensure an adequate sample size for analysis. The material properties of the pFRP profiles are shown in Table 2. The material properties will be used to predict the local buckling behaviour of the pFRP profiles, both theoretically and through the FE model.

The cross-sections of the S125 profiles, obtained at different winding tensions, were prepared for microscopic imaging using a Struers LaboPol by grinding and polishing with 1200 and 320 grit papers, followed by a three-step polishing process. The polishing process included using Dia-Pro for 9 μm on MD-largo plate, DiaPro for 3 μm on MD-DAC cloth, and OP-U Nondry on Neoprene cloth. The cross-section of the sample was examined and imaged using a Leica DMS300 microscope. For more in-depth details and comprehensive image analysis, please refer to [33].

A four-point bending test was conducted on the box section pFRP profiles to investigate their flexural behaviour. Two configurations for S125 and S100 with the span-to-depth ratio of 17.6 and 22.35, respectively, were established to observe pure bending behaviour, as shown in Fig. 2(b). It is worth highlighting that this range of span-to-depth ratio was selected to ensure flexural failure with a lower bound of 16. The loading and supporting plates were equipped with pin-roller steel plates covering 100 mm of the beam length, as shown in Fig. 2(c). Following
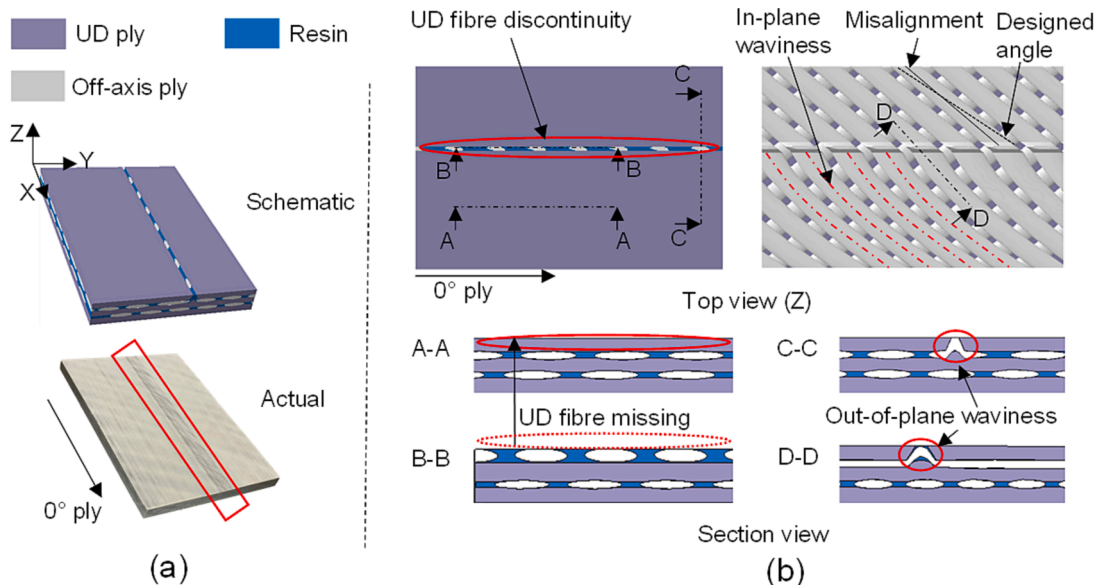
Fig. 3. Schematic of the UD fibre discontinuity; (a) defective sample of the GFRP profile and (b) a description of defects observed in different cutting sections.

Table 2

Mechanical properties of the hollow profiles.

Property			Standard		S125		S100	
					Ave.	St.D.	Ave.	St.D.
Compression		Modulus (GPa)	ASTM D6641		49.1	2.4	50.9	1.5
Tensile	Longitudinal	Modulus (GPa)	ISO 527–4		43.2	1.1	45.1	1.1
		Poisson's ratio			0.3	0.02	0.32	0.02
	Transverse	Modulus (GPa)			13.3	0.6	12.3	0.6
In-plane shear		Modulus (GPa)	ASTM D5379		6.71	0.4	4.70	0.6

ASTM D7249/D7249M, the study tested S125 profiles with three different winding tensions and S100 profiles with medium tension. A quasi-static displacement loading rate of 10 mm/min was applied during testing. Each test group consisted of five specimens, ensuring sufficient data for accurate analysis. The loading was applied to the beam top flange through the loading plates [38]. The deflection of the beam was measured using a Linear Variable Differential Transducer (LVDT) unit.

3. Material imperfection and its characterisation

A typical NUFD induced during the pull-winding process is shown in Fig. 3. In Fig. 3(a), it is evident that there is a noticeable fibre discontinuity on the surface of the pFRP profile's outermost UD ply. Fig. 3(b) presents multiple views of the cross-sections to illustrate the extent of defects further, each revealing typical defects such as fibre misalignment, in-plane waviness, fibre discontinuity, and out-of-plane waviness. In this section, these defects are observable through microscopic analysis, providing valuable insights into the structural characteristics of the profile.

3.1. Formation of fibre waviness

The compaction of the off-axis ply in the thickness direction generates excess length, which can cause in-plane waviness, fibre misalignment within the plane, and out-of-plane waviness outside of the plane. The magnitude of the excess length is related to the thickness change, which depends on the initial winding tension during the pull-winding process. Specifically, higher winding tension leads to a more uniform fibre distribution, while lower winding tension results in more significant NUFD with in-plane and out-of-plane waviness [37]. Fibre waviness can occur during the preform passage through the entry bush into the pultrusion dies, contributing to the formation of the NUFD.

The Filtered Canny Misalignment Analysis (FCMA) method presented by the authors [33] evaluates the in-plane waviness of off-axis plies based on the image process. The scanned off-axis layer was prepared (Fig. 4(a)) through a controlled partial burnout process of the box section profile. Most of the resin evaporated by carefully controlling the furnace temperature and burning time, while a small amount of residual resin was left to preserve the fibre shape. The characterisation results of the in-plane waviness are presented in Fig. 4. This method computes the average local fibre angle relative to the X-axis and the distribution of fibre angles along the Y-axis. According to the localised fibre angle, this
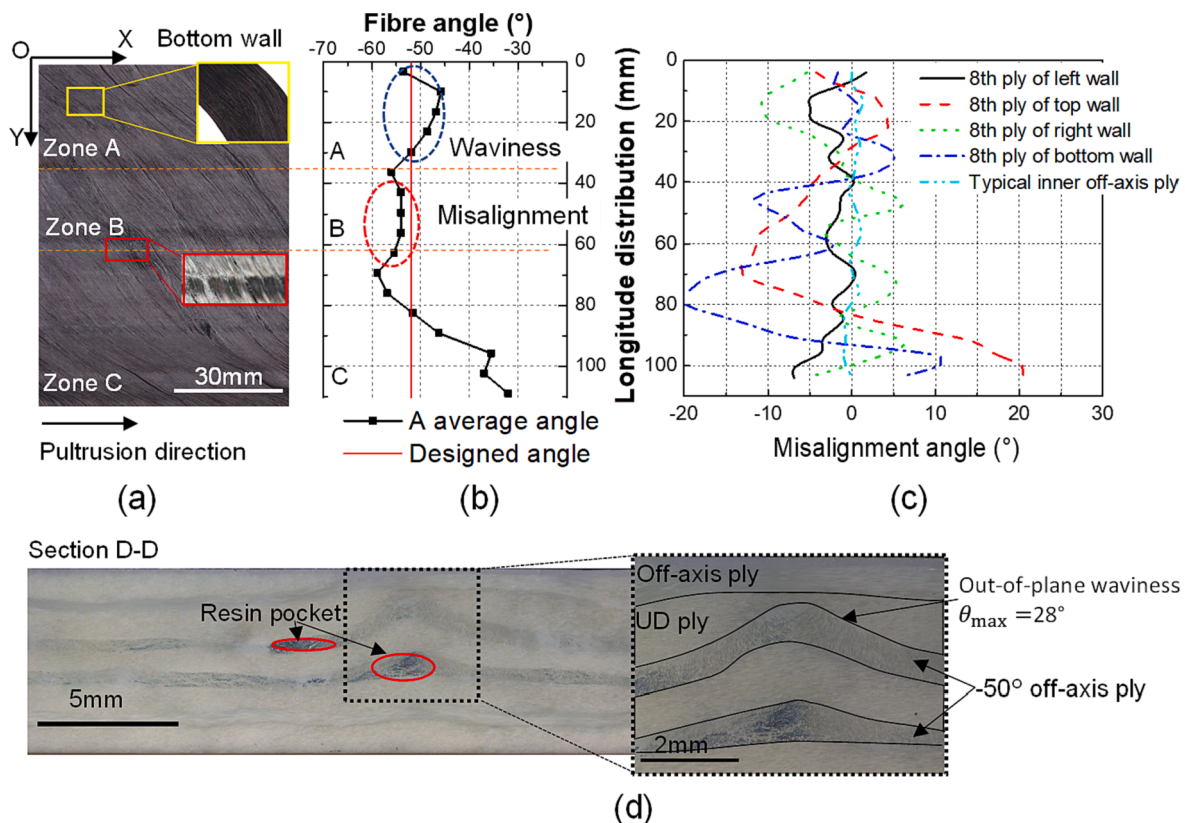
Fig. 4. A typical Fibre waviness in pultruded hollow profiles; (a) scanned image of the off-axis ply, (b) fibre orientation distribution, (c) fibre misalignment angles and (d) out-of-plane waviness of the off-axis ply (+50°).

ply is divided into three regions: zones A, B, and C. The results in Fig. 4 (b) indicate the presence of fibre waviness in zone A, misalignment in zone B, and more severe waviness in zone C. Additionally, the interface between these zones is always accompanied by significant out-of-plane waviness, as indicated by the red square in Fig. 4(a).

Fig. 4(c) compares the misalignment angles of the outermost off-axis ply and a typical inner off-axis ply of a square profile obtained under low winding tension. The results reveal that the outermost ply experiences more significant fibre misalignment, with a maximum angle of around 20°, particularly on top and bottom walls, where the resin is injected into the pultrusion die. These results suggest that resin flow may contribute to the fibre misalignment.

The wound fibres will interact with UD ply when the out-of-plane waviness occurs. Fig. 4(d) shows a cross-section cut along the + 50° direction (similar to section D-D of Fig. 3(b)), which highlights the high level of out-of-plane waviness, with a maximum misalignment reaching 28°. The spaces between the adjacent wound fibres form resin-rich zones. The region with maximum waviness has the outermost UD ply being pushed and split, resulting in discontinuity of UD ply. The absence of the UD ply leads to a reduced local fibre Vf in the cross-section, making it more prone to forming a resin-rich zone.

3.2. Discontinuity of UD ply

The NUFD is a result of the lateral movement of UD fibres, which is caused by the shear force between the UD and wound fibres [39]. Fig. 5 provides a microscopic comparison of the cross-sectional planes of the standard and defective profiles, specifically analysed in sections A-A and B-B (as indicated in Fig. 3(b)). The micrographs offer a detailed visual assessment of the structural differences between the two profiles at a microscopic level. The comparison shows that the outermost UD ply (UD5) is absent in the defective section, as shown in Fig. 5(b). The thickness of the fourth UD ply has decreased by around 70% in the black square of Fig. 5(b). The local fibre Vf of the UD fibre decreased in this area. Moreover, the resin is mainly accumulated in the off-axis ply.

Section C–C in Fig. 5(c) reveals that the resin pocket between the yarn spaces (indicated by red dashed lines) in the off-axis ply of the defective coupon is occupied by fibres, compared to the baseline coupon. The difference can be attributed to the fibre misalignment and the excess length resulting from compaction, which fills the yarn space between the adjacent wound fibres. This effect is particularly prominent in the outer ply, where the excess length is more pronounced than the inner ply.

A previous study by authors discussed the influence of NUFD within the pultruded GFRP profiles on material strength without buckling instability [37]. Results revealed that NUFD caused a local decrease in fibre Vf by approximately 12%, resulting in an 11% reduction in the load capacity of the coupon.

3.3. Characterisation of the non-uniform fibre distribution

The change in the area of the UD ply along the cross-section was used to characterise the NUFD. Based on the findings in Fig. 5, it is evident that the waviness of the off-axis ply results in the actual displacement of the UD fibres, leading to variations in the local area of the UD ply. If neglecting any changes in the gap between the UD fibres, the area of the UD ply becomes a reliable indicator of the NUFD along the cross-section, serving a similar purpose as the UD fibre Vf. The cross-section of the box section profile can be divided into grids, allowing for the characterisation of the variations in the area of the UD ply, as shown in Fig. 6(b). Then, the local fibre Vf can be assessed by Eq. (1).

$$V_i = (1 + \alpha)V_{Basic} \tag{1}$$

where α is the rate of change in the proportion of identified UD ply area compared to the average proportion of UD ply area in the cross-section. V_{Basic} is the average fibre Vf of the cross-section.

The pultruded profile's cross-section was ground, polished, and then imaged. Image analysis was performed using MATLAB to identify the UD ply based on the contrast between UD fibre and wound fibres. Fig. 6(a) shows the identified UD fibre ply at the corner, marked in blue, as a
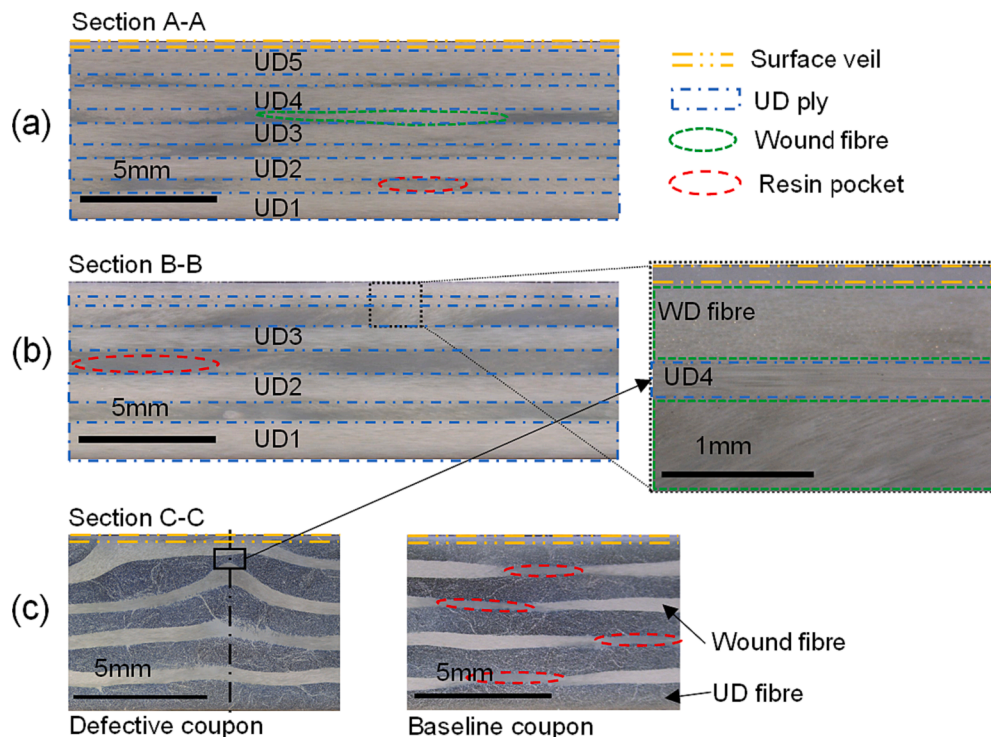

Fig. 5. Characterisation of the typical NUFD at different cutting sections; (a) section A-A, (b) section B-B, and (c) section C–C. The definition of section direction refers to Fig. 3.
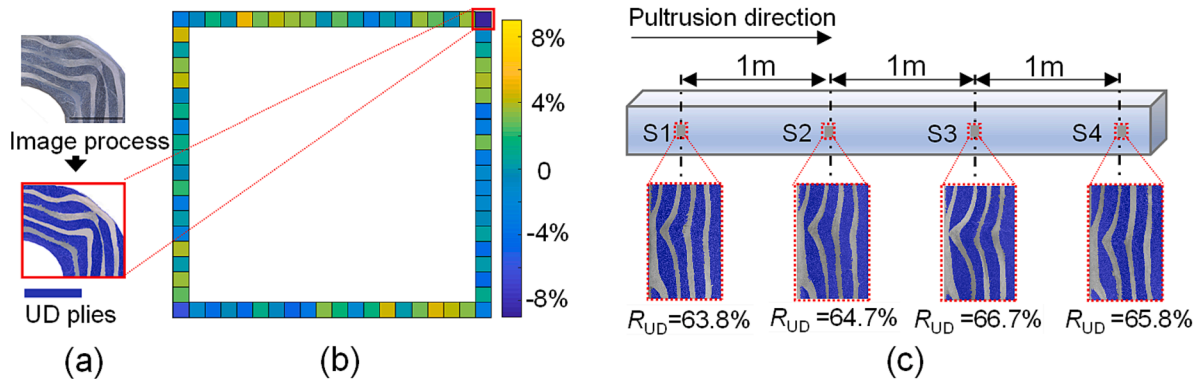
Fig. 6. Measurements of the non-uniform fibre distribution; (a) Segmented UD plies in a single measurement grid, (b) relative V_f deviation of the profile cross-section, and (c) segmented UD plies in the same cross-sectional grid but the different locations along the pultrusion direction.

measurement grid of the cross-section. Seventy-six evenly spaced locations (grids) along the cross-section were sampled to calculate the area of the UD ply using this methodology. Fig. 6(b) shows the relative deviation of the ith UD ply area R_i that is calculated by Eq. (2) across the whole box section.

$$R_i = \frac{S_i - S_A}{S_A} \tag{2}$$

where S_i is the ith area of the identified UD ply; and S_A is the average area of the UD ply. A negative R_i indicates that this region has fewer UD fibres, leading to the NUFD. The positive R_i indicates that the lateral moved UD fibres fill the yarn space in off-axis plies.

Fig. 6(c) illustrates the stability of the UD fibre distribution along the pultrusion direction. Four grids of the defective area were observed at one-metre intervals, and the distributions of the UD fibre were shown. Each grid has an identical UD ply area with out-of-plane waviness and UD fibre discontinuity. The UD ply area ratio (R_{UD}) is close to each other, with a standard deviation of 1.3%. Therefore, the defects along the pultrusion direction were uniform.

4. Rotational restraint of the flange support

The contribution of the flange-web junction to the elastic rotational stiffness of flange edge support has been ignored in conventional

methods [39]. However, the impact of this junction on the FLB behaviour of FRP sections has been demonstrated in some studies, which showed that a weak junction could lead to premature failure of the entire profile [17,40]. In this study, the defect that occurs in the flange-web junction will be investigated to assess the influence on the constraint coefficient.

Fig. 7(a) shows the isolated segment BC (Fig. 2 (b)) of the box section to demonstrate the FLB according to elastic plate theory. When the length of L_x is much larger than L_y, the analytic solution for critical buckling stress can be calculated by Eq. (3) [39].

$$\sigma_{cr} = \frac{\pi^2}{t_f L_y^2}\left[\alpha\sqrt{D_{11}D_{22}} + \beta(D_{12} + 2D_{66})\right] \tag{3}$$

Where D_{ij} is the plate flexural stiffness parameter and can be calculated based on Appendix A and Table 2; t_f is the wall thickness; α and β are dependent on the boundary condition of the edge, which accounts for the rotational stiffness of the flange support. When the long edge of the plate is rotationally restrained, α and β are calculated by Eq. (4) and Eq. (5), respectively.

$$\alpha = 2\sqrt{1 + 4.139\xi} \tag{4}$$
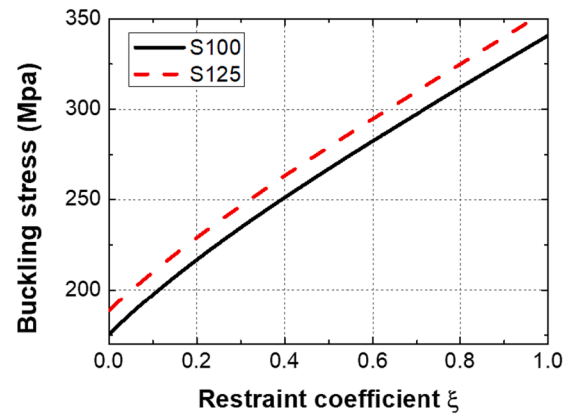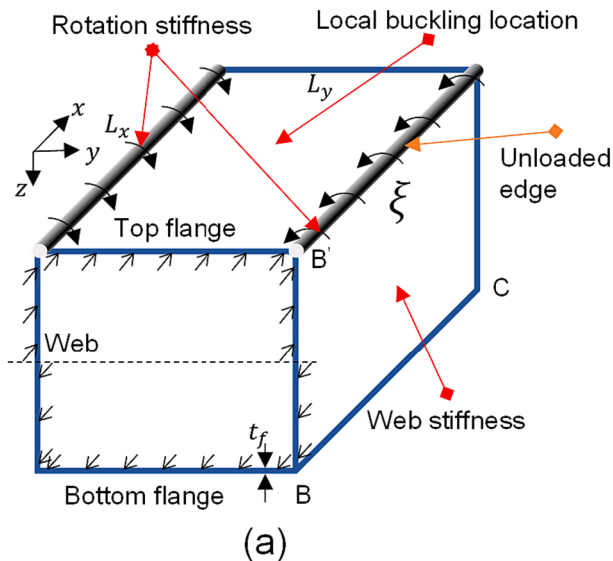
$$\beta = 2 + 0.62\xi^2 \tag{5}$$

Fig. 7. Elastically restrained plate under the bending test; (a) schematic loading condition of section BC, and (b) the relationship between rotational restraint coefficient and buckling stress.

Then,

$$\sigma_{cr} = \frac{\pi^2}{t_f L_y^2} \left[2\sqrt{1+4.139\xi} \sqrt{D_{11}D_{22}} + (2+0.62\xi^2)(D_{12}+2D_{66}) \right] \quad (6)$$

ξ is a parameter that reflects the restrain of the unloaded edge. When $\xi = 0$, the unloaded edge is seen as simply supported. When $\xi = 1$, the unloaded edge is fully clamped. Fig. 7(b) displays the correlation curve between the rotational restraint coefficient and the buckling stress. This curve can be utilised to determine the inverse coefficient when provided with the buckling stress value.

5. Finite element modelling and validation

5.1. Modelling

The material non-linearity due to the inhomogeneous fibre distribution posed a challenge for converging the FE model. To overcome this, Abaqus/Explicit was employed to study the local buckling and post-local buckling behaviour under bending. The loading rate was controlled with a smooth step to increase the accuracy of the simulation, which aimed to replicate the results of a pseudo-static test [41].

The composite profiles were modelled, neglecting the delamination between plies due to the computational cost and accurately matched experimental results [22,42,43]. This is because the profiles are confined by continuous inclined fibre plies and closed geometry; hence, the inter-laminar failure analysis in this model was neglected. Transverse shear and tensile damage in the matrix were used to track the delamination propagation [44], and the Hashin damage model was used to simulate the intra-laminar failure. Table 3 lists the strength limits and fracture energy values [22,45]. These strength limits and fracture energy values were verified against extensive experimental programs on structural-level size specimens of the same profile (same fibre and resin type with different dimensions) under compression and bending loadings in previous studies [20,22,43,46,47]. The X, Y, and S refer to the longitudinal, transverse, and shear strength values, respectively, and subscripts T and C indicate tension and compression, respectively. In the double subscript notation of the fracture energy, the first subscript refers to the longitudinal or transverse directions, and the second subscript refers to tension or compression.

The simulation employed 8-node quadrilateral in-plane general-purpose continuum shells (SC8R) and used a 5 mm mesh with six elements through the thickness according to the mesh sensitivity study. A rigid body was employed and tied to the beam to simulate the loading plate. The surface between the supporting plate and beam is defined in normal and tangential directions. A friction coefficient of 0.3 was adopted to simulate friction between the beam and the steel plate [48]. The boundary and loading conditions were applied through the reference point of the rigid body, as shown in Fig. 8(a).

The material properties of the composites discussed in Section 3, such as modulus and strength, were not uniform along the cross-section due to the NUFD. The simulation considered this inhomogeneity by defining a coordinate-related fibre Vf in the predefined field in Abaqus, as shown in Fig. 8(a). The NUFD along the pultrusion direction is observed to be consistent in Section 4. Therefore, the material properties along the Z direction were kept constant. The relationship between the fibre Vf and elastic and shear moduli is calculated using the mixture rule [44], which is provided in Appendix B. The fibre and matrix material

Table 3
Strength limits and fracture energy values of the pultruded lamina.

Strength limits (MPa)							Fracture energy (N/mm)			
X^T	X^C	Y^T	Y^C	S^L	S^T		G_{LT}	G_{LC}	G_{TT}	G_{TC}
803	548	43	187	64	50		92	79	16	16

properties are listed in Table 4 [31,49].

5.2. Model verification

The FE model was validated against experimental results, including load–deflection curves and failure modes. The flange of the S125 profile was observed to buckle before the web, as the flange ratio of buckling stress-to-longitudinal modulus $(\sigma_{cr})/(E_L)$ was lower than the web ratio. Both the experiments and FE model confirmed this phenomenon.

The FE model results align with the experimental results, as depicted in Fig. 8(b). The load–deflection curves of S125 and S100 profiles with varying winding tensions are shown, exhibiting linear elastic behaviour until reaching the maximum load. The trend seen in both the slope of the load curve and load capacity supports the use of the changing fibre Vf to reflect the mechanical performance change.

The local buckling of the top flange can be seen in the experimental and numerical results at the ultimate load point, as shown in Fig. 9(a). The waviness extent indicates this local buckling observed before the beam collapses. The numerical result of the localised waviness can be traced by the compressive damage of the fibres and tensile damage of the matrix, which aligns with the experimental result. Afterwards, the fibre damage on the top flange causes the collapse and subsequent spalling and delamination of the top flange and webs. The damage-shear envelope of the FE model (DAMAGEMT) is used to capture the delamination process, as shown in Fig. 9(b). Both the numerical and experimental results indicate that the collapse occurs at the mid-span of the beam.

6. Results and discussion

6.1. Influence of wound fibre tension on NUFD development

The NUFD in the profiles is a result of various winding tension during the pull-winding process. The image analysis results with three different degrees of NUFD are shown in Table 5. The average UD ply ratio R of three sets of samples is similar across the whole section, despite the different winding tensions. This is because the fibre delivery in the pull-winding process (Fig. 1(a)) is consistent among the three samples, meaning they contain the same amount of fibre. Therefore, using the image analysis method to evaluate the variation of the UD fibre Vf along the cross-section is reasonable. It can be observed that the ratio of UD fibres at the corner is lower compared to wall fibres, suggesting that the UD fibres at the corner are prone to moving away during compaction.

The fibre Vf distribution along the cross-section is depicted in Fig. 10, which is calculated based on the change in the UD ply area. The minimum fibre Vf occurs at the corners for low and high-tension samples, while it occurs at the web for samples under medium tension. The outermost off-axis ply experiences the most severe out-of-plane waviness, resulting in more server NUFD in the outer UD ply than the inner UD ply. This phenomenon is attributed to the greater excess length generated by the outermost off-axis ply during the pultrusion process. The excess length can be assessed by the thickness change between the dry preform and the final product. When the winding tension is lower, the thickness change is greater. With the movement of UD fibres, the accumulation of neighbour UD fibres results in a high local fibre Vf. These results were defined as a field variable in the Abaqus subroutine to reflect changes in mechanical performance. The code is supplied as supplementary material to this paper.

The ultimate loads with different NUFDs in Fig. 11 demonstrate the ability of the FE model to accurately reflect the impact of NUFD on the mechanical performance of the profiles. The impact of NUFD on the ultimate load of the low-tension sample is around 5%, while the corresponding variation in fibre Vf is around 13%. The existence of NUFD results in a decrease in load capacity compared to the FE mode with a homogenous fibre distribution. The medium-tension sample has the least load capacity reduction, as no significant NUFD occurs at the corner, as seen in Fig. 10.
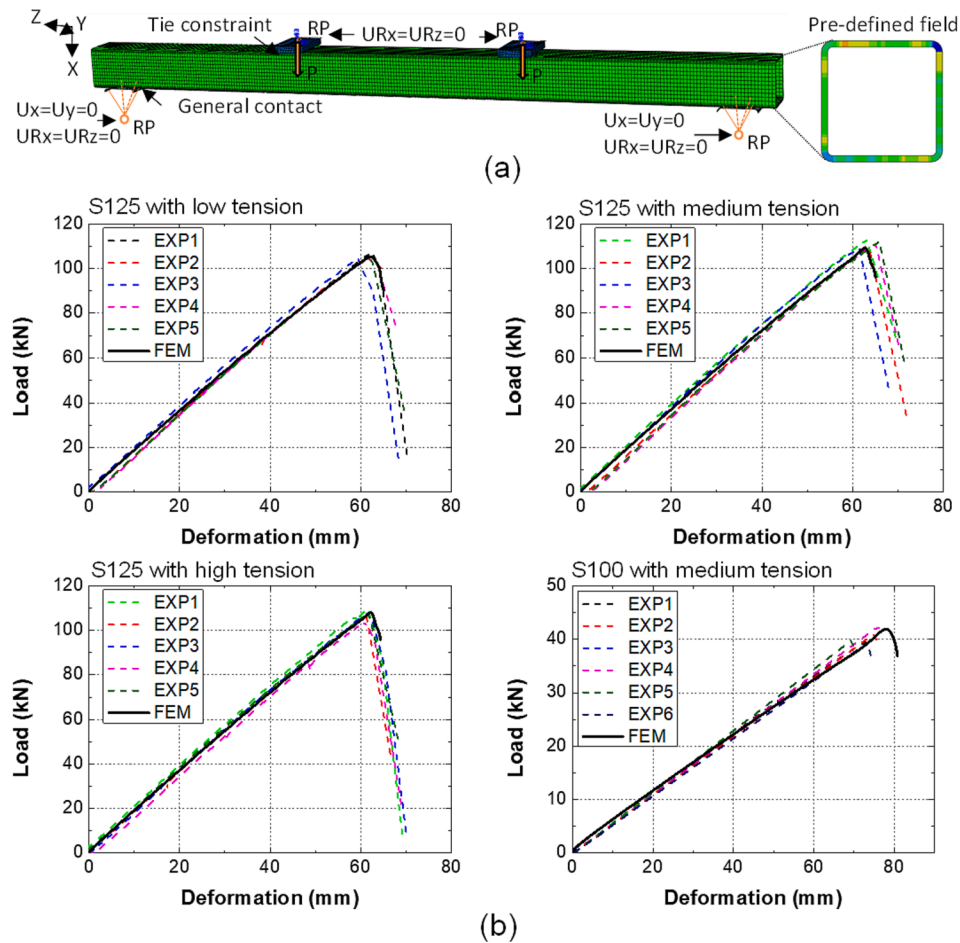
Fig. 8. FE analysis; (a) boundary condition and predefined field of fibre Vf, and (b) FE modelling vs experimental load–deflection curves.

Table 4
Modulus of fibre and matrix.

Material	Property	Symbol	Value
Fibre	Young's elastic modulus/GPa	E_f	73
	Shear elastic modulus/GPa	G_f	30
	Poisson's ratio	υ_f	0.22
Matrix	Young's elastic modulus/GPa	E_m	3.4
	Shear elastic modulus/GPa	G_m	1.3
	Poisson's ratio	υ_m	0.35

6.2. Rotation stiffness at the corner

The rotational restraint coefficient ξ is a crucial parameter for determining the buckling behaviour of box section beams under axial compression. According to Qiao et al. [50], the analytical solution for ξ can be calculated for box section beams under axial compression. In their study, it was found that ξ equals 0 when the width of flange and web is equal, indicating that buckling occurs simultaneously in the flange and web. However, in the case of S125 and S100 beams used in this research, which have equal widths for the flange and web, the experimental results were found to be closer to the predicted value of $\xi = 1$. This observation is based on the comparison (pred/exp) between the experimental data shown in Table 6. This analytical solution ξ for axial compression cannot be applied directly because only the top flange and partial web are under the axial compression in the four-point bending test.

This research evaluates the effect of NUFD on the rotational restraint coefficient ξ. The exact value of ξ is not determined, but rather a

description of the reduction factor is provided when NUFD is introduced. Based on the experiment buckling value, the theoretical value of ξ can be calculated according to Fig. 7(b). The results in Table 6 show that the inverse values of both beams are far from zero, indicating that the unloaded edge L_y is partially constrained instead of simply supported. The constraint coefficient value is influenced by factors such as flange edge support [15], corner geometry [21], and imperfection [17]. This study assessed the effect of imperfection on buckling load by the change of fibre Vf.

6.3. Effect of NUFD on different failure modes

The samples of S125 and S100 exhibit FLB as a failure mode. According to previous research [43], increasing the wall thickness of S125 from 6.2 mm to 10 mm will convert the failure mode from FLB to compressive material failure. Fig. 12 illustrates the geometry of the thickened S125 profile and its failure due to the material strength limitation.

The study quantifies the impact of NUFD on the flexural strength of composite beams using the validated FE model, as discussed in Section 5. Fig. 13(a) shows the defect positions, including the wall and corner defects. The NUFD is represented by the relative decrease in UD fibre Vf in the defective area (V_{defect}), as below.

$$R_{Vf} = \frac{V_{defect} - V_{Basic}}{V_{Basic}} \times 100\% \tag{7}$$

where V_{Basic} is the basic fibre Vf of 0.625. The normalised maximum load for the box section profiles with NUFD is calculated based on the maximum load obtained from a profile with uniform material ($R_{Vf} = 0$).
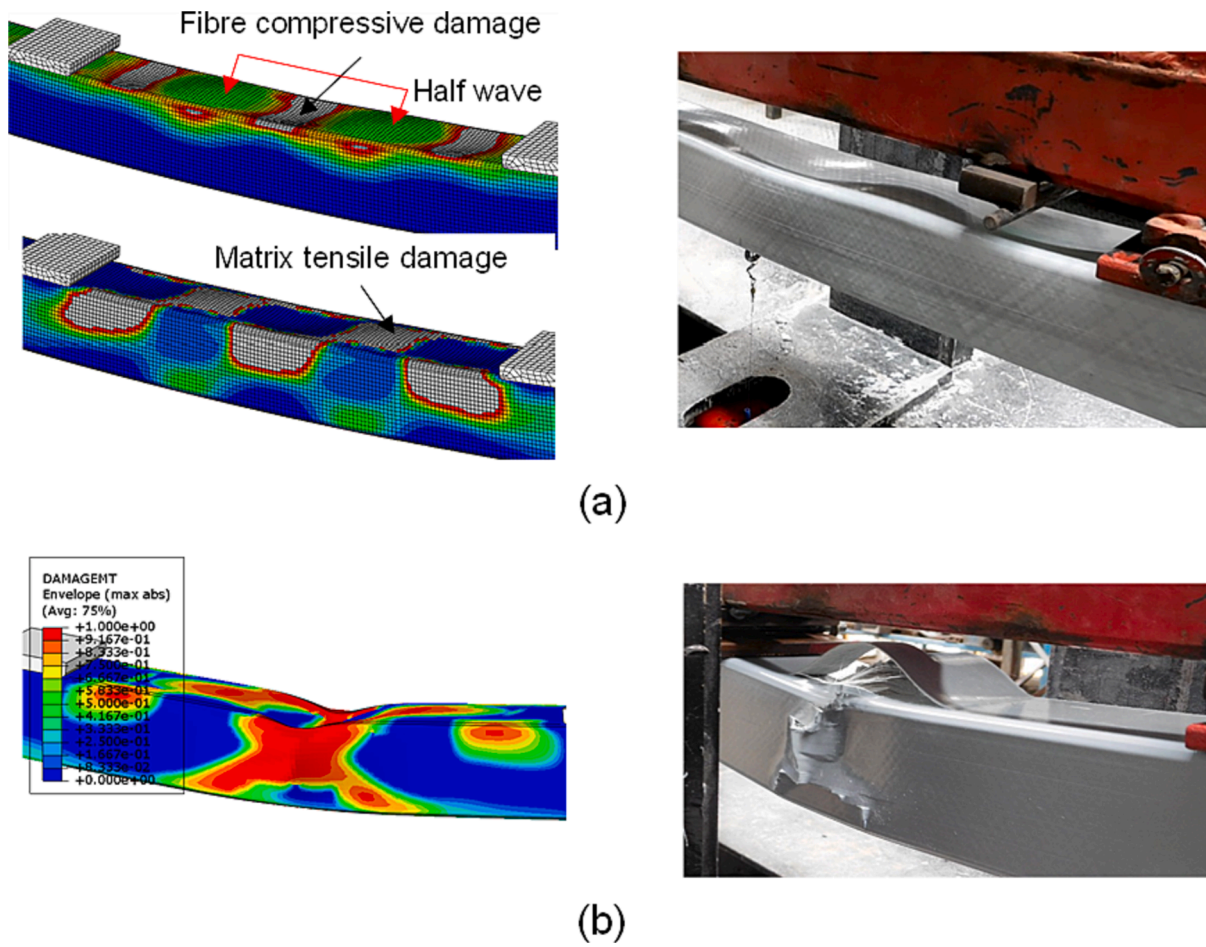
Fig. 9. Numerical vs experimental failure mode of the S125 beam at (a) the ultimate load point and (b) collapse.

Table 5
The ratio of the UD ply area to the profile cross-sectional area.

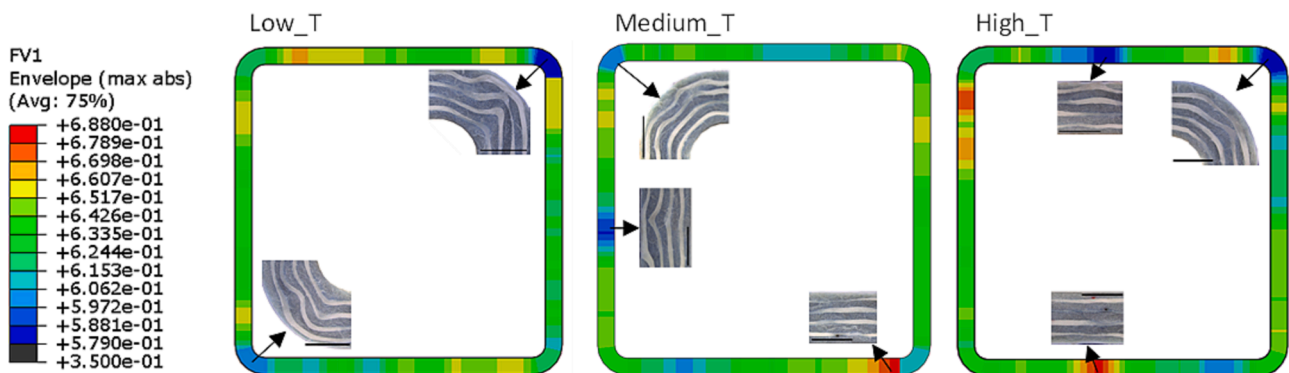| Samples	Wall (%)			Corner (%)			Whole (%)	Thickness change (mm) (St.D.)
	Average (St.D.)	Maximum deviation		Average (St.D.)	Maximum deviation		Average (St.D.)	
Low	73.3 (2.0)	5.1		69.1 (2.1)	9.1		72.91 (2.32)	3.2 (0.1)
Medium	72.3 (2.3)	7.7		70.7 (2.3)	5.0		72.12 (2.31)	2.5 (0.2)
High	72.3 (2.9)	11.2		70.4 (3.1)	8.6		72.14 (2.97)	2.0 (0.2)

Fig. 10. The fibre Vf distribution in the cross-sections of the experimental samples with low, medium, and high winding tension.
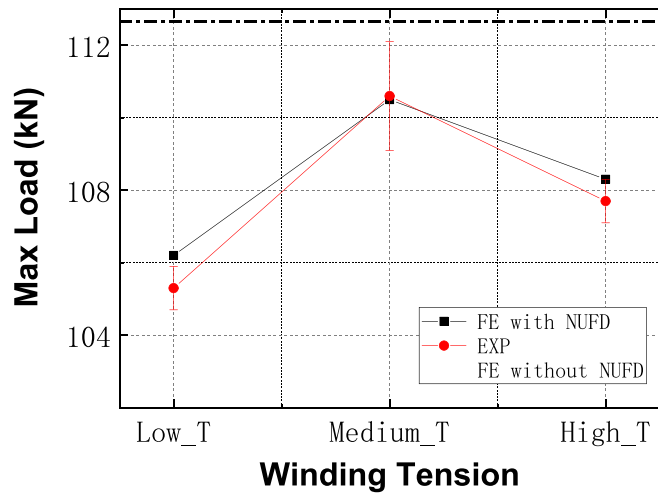
Fig. 11. Comparison of load capacity between FE model and experiment of S125 profiles with different NUFDs.

A value of −100% for R_{Vf} indicates the complete absence of UD fibres in the defective area replaced by resin, while the wound fibres remain unchanged. The width of the wall defect area is 10 mm and has the same area as the corner defects. These defects are analysed separately, and all other areas are assumed to be uniform.

The result of the FE model, as shown in Fig. 13(b), demonstrates the influence of NUFD on the ultimate load of the S125 beam. The NUFD only affected the ultimate load without any change in the failure mode by FLB. Considering the worst-case scenario, when the fibre Vf decreases by 100%, the impact of flange and web defects is small, within 3%. However, the ultimate load decreases by 8% and 14%, respectively, when there are one and two top-corner defects. The difference highlights the contribution of top-corner defects to local buckling, as the NUFD at corners has a negative effect on the rotational restraint coefficient.

The results are similar for the S100 samples, with the corner defects having a more significant impact on the ultimate load by a maximum 20% reduction compared to the top flange defects, as they exhibit the same failure mode, as shown in Fig. 13(c). The load capacity of S100 and S125 samples decreases linearly with the relative decrease in corner fibre Vf.

To examine the impact of NUFD on compressive material failure mode, the thickness of the S125 profile is increased to 10 mm, and the resulting structure is named 'thickened S125 beam.' The thickened S125 profile experiences a compressive material failure in the top flange due to the material strength limitation and reduced tendency to buckle. The load capacity of the thickened S125 beam with top corner and flange defects shows a decrease, which has a similar magnitude of decline with R_{Vf}, as shown in Fig. 13(d). The top flange performs differently from the basic S125 beam. The web and bottom NUFDs do not significantly affect load capacity as the basic S125 beam. Furthermore, when the fibre Vf at the corner increases ($R_{Vf} > 0$), the improvement in strength for compressive failure mode is 0.4%, while for local FLB mode, it is 3.1%. This improvement is due to an increase in the restraint coefficient for

FLB. By comparing the effect of NUFD on different failure modes, it can be seen that local buckling is more sensitive to NUFD. This finding explains why non-uniform fibre packing over cross-section has a limited effect on compressive material strength [30].

The axial stress distribution in the middle plane of the S125 beam, at 97% of the ultimate load (just before failure), is presented in Fig. 14(b). The presence of NUFD affects stress distribution. When the fibre Vf decreases in a defective area, the stress is lower in defective areas than in the uniform material beam. However, a top flange defect with a low fibre Vf causes a reduction in bending stiffness and moment, while a corner defect reduces the rotation stiffness. These factors contribute to a higher buckling load in the former case and a lower buckling load in the latter case, as demonstrated in Fig. 13(b) and Fig. 13(c).

Fig. 14(c) shows the change in logarithmic strain with the fibre Vf at the corner in the tangential direction of the cylindrical coordinate at the same loading displacement point. As the corner fibre Vf increases, the strain of the top flange decreases due to the growing rotational stiffness, which can obtain higher local buckling capacity. Therefore, avoiding a lower Vf at the corner is recommended to obtain a higher load capacity. Alternatively, the corner area can be increased to enhance the load capacity [46].

6.4. Rotational stiffness reduction factor for NUFD at corners

The results of the ultimate load of the S125 and S100 beams obtained from the FE model can be transformed into rotational restraint coefficients (Fig. 7(b)). The normalised restraint coefficient is the ratio of the calculated coefficient from the non-uniform model and the uniform model, which can represent the resistance reduction factor. This
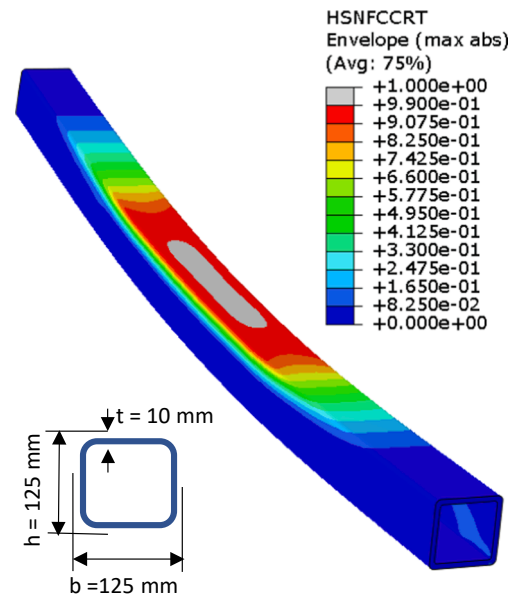

Fig. 12. The cross-sectional geometry of the thickened S125 profile and the compressive material failure mode.

Table 6
The critical buckling stress determined by experiment and analytical prediction.

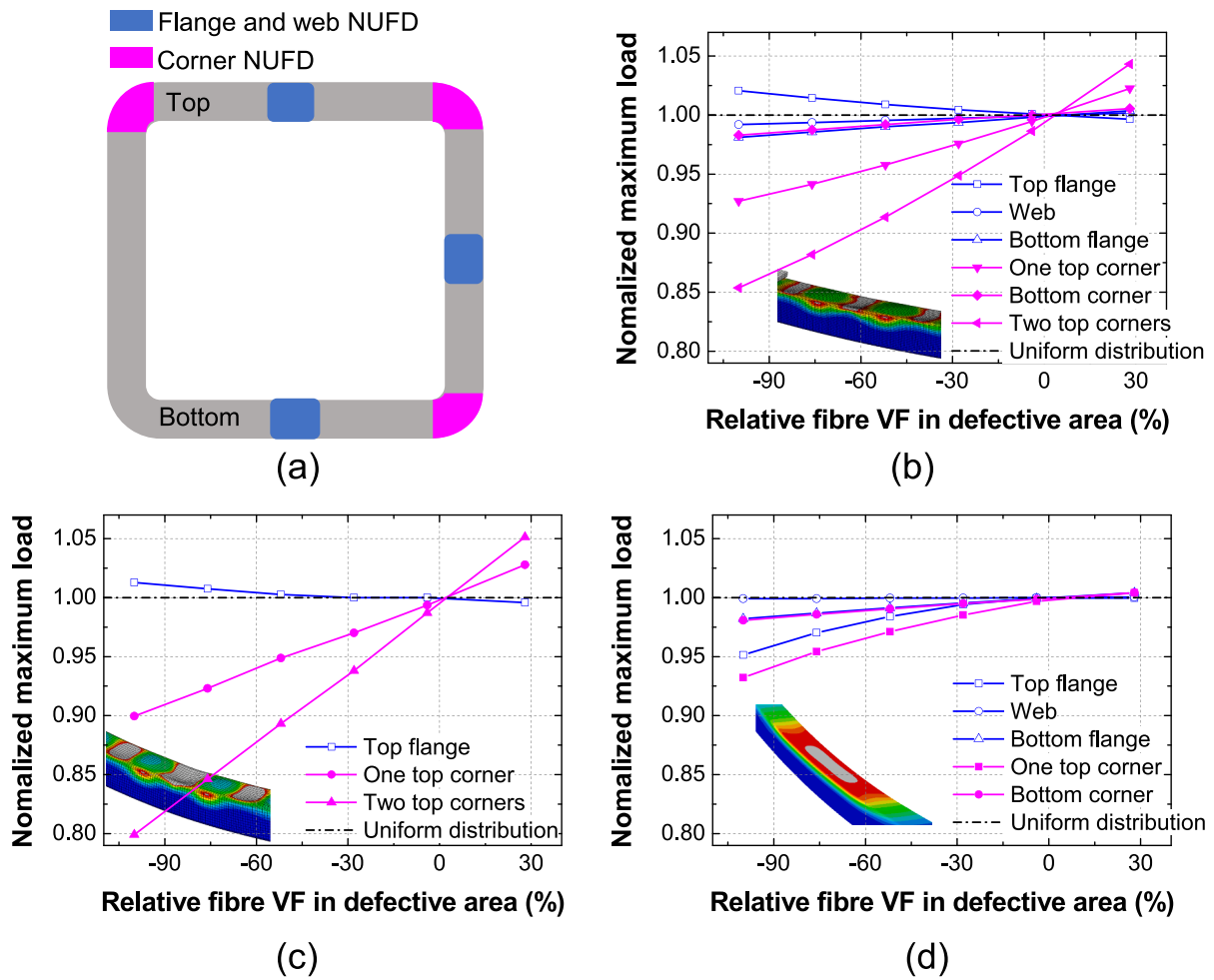| Label	Exp.	Analytical				Inversed
		$\xi = 0$		$\xi = 1$		
	σ_{cr}(MPa)	σ_{cr}	pred/exp	σ_{cr}	pred/exp	ξ
S125 Low_T	322.6	188.5	0.58	354.7	1.1	0.79
S125 Medium_T	338.8	188.5	0.55	354.7	1.05	0.89
S125 High_T	330.0	188.5	0.57	354.7	1.07	0.83
S100 Medium_T	308.4	175.7	0.57	340.9	1.10	0.78

Fig. 13. The influence of local NUFD on the load capacity; (a) NUFD position; (b) effect on S125 beam, (c) S100 beam and (d) thickened S125 beam.
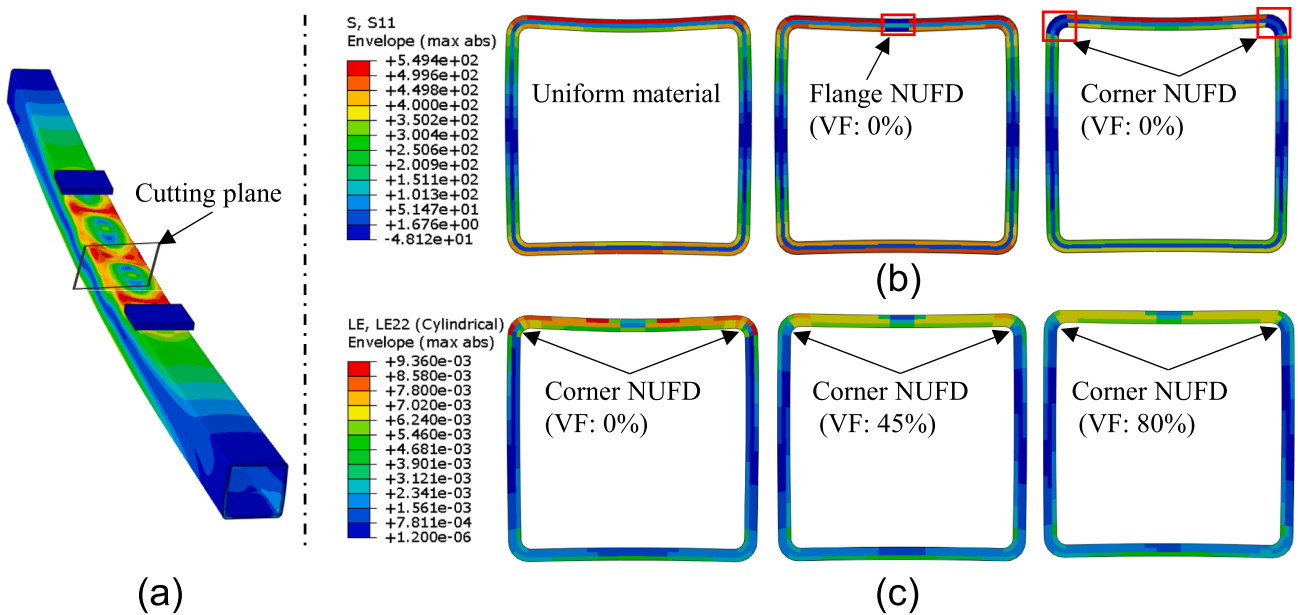

Fig. 14. The influence of local NUFD on the stress and strain of the S125 beam; (a) the position of the cutting plane, (b) stress comparison at different NUFD locations, and (c) strain distribution under the same loading displacement.
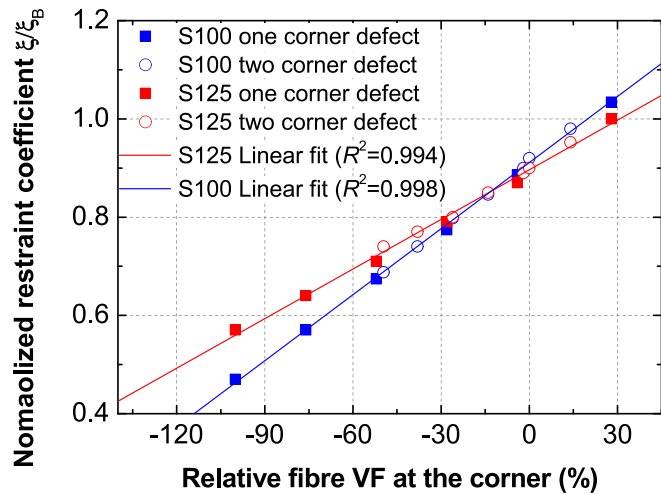
Fig. 15. The influence of corner NUFD on the rotational restraint coefficient of the S100 and S125 beams.

relationship is presented in Fig. 15, where a linear correlation can be observed between the corner fibre Vf and the rotational restraint coefficient for both profiles.

A linear regression analysis was carried out on the S100 and S125 data to determine their slope and intercept values, as shown in Fig. 15. The slope represents the sensitivity of the box section structure to the corner NUFD, while the intercept represents the rotational restraint coefficient when the corner material is uniform ($R_{Vf} = 0$). The analysis revealed that the S100 beam has a higher slope (0.44) than the S125 beam (0.34), primarily due to its higher UD fibre content ratio (Table 1). Moreover, the intercept values for both profiles are similar, 0.91 for S100 and 0.90 for S125, indicating that the two different profiles have the same rotational restraint coefficient in a uniform material, despite their different layups and geometries. For reference, a decrease of 30% in the corner fibre Vf results in an approximate reduction of 21% of the rotational restraint coefficient for both profiles. This regression model can be utilised during the early stages of material design evaluation and manufacturing quality control.

7. Conclusion

This study investigates the impact of non-uniform fibre distributions (NUFD) on the load capacity of box-section composite profiles under bending, focusing on the flange local buckling (FLB) failure mode and compressive material failure. The samples manufactured using different winding tensions exhibit a 9% NUFD deviation at the corner. Based on the classic plate theory, the study highlights that the rotational restraint coefficient under bending differs from that under axial compression. The rotational restraint coefficient for a square box section profile during bending is close to 1.0, unlike the established value in literature, which is close to 0 during axial compression [50]. This difference is because not all flanges and webs are under axial compression during the four-point bending test. The results show the significance of considering this difference in the design-for-manufacturing stage.

The samples with different NUFDs were manufactured using different winding tensions, resulting in a 5% variance in load capacity. To better comprehend how NUFD influence the local buckling capacity, NUFD modelling was implemented by changing the fibre Vf along the cross-section and considering it as an input in the FE model. The model

with NUFD more accurately predicts the local buckling load compared to the uniform material model. A parametric study was then conducted to analyse the effect of the NUFD location on the buckling load. Results indicate that corner NUFD decreases the FLB capacity by up to 20%, while flange NUFD increases it slightly by up to 3% in cases where the UD ply within the defective area is filled with resin. This reduction in load capacity is attributed to the decreased rotational restraint coefficient at the corner. Conversely, the effect of NUFD location across the section was found insignificant in beams dominated by a compressive failure of fibre, at which the ultimate material strength is reached without buckling instability.

The decrease in local buckling load was proportional to the relative decrease in fibre Vf at the corner, as indicated by the regression model. This model can be used in the early stages of material design evaluation to estimate the effect of the NUFD on the flexural behaviour of box section pFRP beams. Numerical results from the S100 and S125 profiles indicate that the linear trend observed in the regression model is independent of profile geometry and fibre layup. Additionally, when the fibre Vf at the corner is reduced by 30%, it leads to an approximate 21% decrease in the rotational restraint coefficient for both profiles. This finding can be used as a reference for evaluating the effects of material imperfection. Considering the NUFD at the corner, it was concluded that using $\xi = 0$ (as established by EUR 27666 [51]) is a conservative prediction.

Further investigations would be required to incorporate the rotational restraint coefficient and its relationship with the associated NUFD in the laminated classical theory, which is reflected in a linear trend in this research. The current FE model neglects delamination between plies which is worth to be investigated in further. Additionally, it would be valuable to explore the effect of other manufacturing parameters, such as resin flow and curing conditions, on NUFD development and its impact on the mechanical behaviour of composite profiles.

CRediT authorship contribution statement

Songming Qi: Conceptualization, Methodology, Software, Investigation, Writing – original draft, Writing – review & editing. **Omar Alajarmeh:** Formal analysis, Methodology, Writing – review & editing. **Mohammad Alhawamdeh:** Software, Methodology, Writing – review & editing. **Tristan Shelley:** Methodology, Writing – review & editing. **Peter Schubel:** Supervision, Writing – review & editing. **Kendric Rendle-Short:** Formal analysis, Investigation, Resources. **Xuesen Zeng:** Supervision, Conceptualization, Methodology, Writing – review & editing.

Declaration of Competing Interest

The authors declare that they have no known competing financial interests or personal relationships that could have appeared to influence the work reported in this paper.

Data availability

The data has been in the article.

Appendix A. . Plate flexural stiffness parameters

$$D_{11} = \frac{E_L t^3}{12(1 - \upsilon_{12} \cdot \upsilon_{21})} \tag{A.1}$$

$$D_{22} = \frac{E_T t^3}{12(1 - \upsilon_{12} \bullet \upsilon_{21})} \tag{A.2}$$

$$D_{12} = \upsilon_{12} D_{12} \tag{A.3}$$

$$D_{66} = \frac{G t^3}{12} \tag{A.4}$$

E_L: Longitudinal modulus of elasticity

E_T: Transverse modulus of elasticity.

G: Shear modulus.

t: Thickness.

υ_{ij}: Poisson's ratio.

Appendix B. . The rule of the mixture of fibre and matrix

$$E_{11} = V_f E_f + (1 - V_f) E_m \tag{B.1}$$

$$E_{22} = \frac{E_f E_m \left[V_f + \eta_2 (1 - V_f) \right]}{E_m V_f + E_f \eta_2 (1 - V_f)} \tag{B.2}$$

$$\upsilon_{12} = \upsilon_f V_f + (1 - V_f) \upsilon_m \tag{B.3}$$

$$G_{12} = G_m \left(\frac{(1 + V_f) G_f + (1 - V_f) G_m}{(1 - V_f) G_f + (1 + V_f) G_m} \right) \tag{B.4}$$

$$G_{23} = G_m \left(\frac{V_f + (1 - V_f) \eta_4}{\eta_4 (1 - V_f) + V_f G_m / G_f} \right) \tag{B.5}$$

$$\eta_2 = \frac{0.2}{1 - \upsilon_m} \left(1.1 - \sqrt{\frac{E_m}{E_f}} + \frac{3.5 E_m}{E_f} \right) (1 + 0.22 V_f) \tag{B.6}$$

$$\eta_4 = \frac{3 - 4\upsilon_m + G_m / G_f}{4(1 - \upsilon_m)} \tag{B.7}$$

E_{11}: modulus of elasticity in the fibre direction

E_{22}: modulus of elasticity in the direction transverse to fibres.

G_{12}: in-plane shear modulus.

G_{23}: out-of-plane shear modulus.

υ_{12}: in-plane Poisson's ratio.

V_f: fibre volume fraction.

E_f: Young's elastic modulus of the fibre.

G_f: Shear elastic modulus of the fibre.

υ_f: Poisson's ratio of the fibre.

υ_m: Poisson's ratio of the matrix.

E_m: Young's elastic modulus of the matrix.

G_m: Shear elastic modulus of the matrix.

Appendix C. Supplementary material

Supplementary data to this article can be found online at https://doi.org/10.1016/j.compstruct.2023.117695.

References

[1] Guades E, Aravinthan T, Islam M, Manalo A. A review on the driving performance of FRP composite piles. Compos Struct 2012;94:1932–42.

[2] Uddin N. Developments in fiber-reinforced polymer (FRP) composites for civil engineering. Elsevier 2013.

[3] Gand AK, Chan T-M, Mottram JT. Civil and structural engineering applications, recent trends, research and developments on pultruded fiber reinforced polymer closed sections: a review. Front Struct Civ Eng 2013;7:227–44.

[4] Fangueiro R. Fibrous and composite materials for civil engineering applications. Elsevier 2011.

[5] Madenci E, Onuralp Özkılıç Y, Gemi L. Buckling and free vibration analyses of pultruded GFRP laminated composites: Experimental, numerical and analytical investigations. Compos Struct 2020;254:.

[6] Debski H, Rozylo P, Teter A. Buckling and limit states of thin-walled composite columns under eccentric load. Thin-Walled Struct 2020;149.

[7] Czapski P, Lunt AJG. The influence of manufacturing on the buckling performance of thin-walled, channel-section CFRP profiles—An experimental and numerical study. Thin-Walled Struct 2023;184:110475.

[8] Ascione L, Berardi VP, Giordano A, Spadea S. Pre-buckling imperfection sensitivity of pultruded FRP profiles. Compos B Eng 2015;72:206–12.

[9] Matthews FL, Davies G, Hitchings D, Soutis C. Finite element modelling of composite materials and structures. Elsevier 2000.

[10] Cardoso DCT, Harries KA, Batista EdM. Compressive strength equation for GFRP square tube columns. Composites Part B: Engineering. 2014;59:1-11.

[11] Kollár L, Springer G. Thin Plates. In: Springer GS, Kollár LP, editors. Mechanics of Composite Structures. Cambridge: Cambridge University Press; 2003. p. 89–168.

[12] Arani AG, Maghamikia S, Mohammadimehr M, Arefmanesh A. Buckling analysis of laminated composite rectangular plates reinforced by SWCNTs using analytical and finite element methods. J Mech Sci Technol 2011;25:809–20.

[13] Cardoso DCT, Harries KA, Batista EdM. Closed-form equations for compressive local buckling of pultruded thin-walled sections. Thin-Walled Structures. 2014;79: 16-22.

[14] Qiao P, Davalos JF, Wang J. Local buckling of composite FRP shapes by discrete plate analysis. J Struct Eng 2001;127:245–55.

[15] Kollár LP. Local buckling of fiber reinforced plastic composite structural members with open and closed cross sections. J Struct Eng 2003;129:1503–13.

[16] Ascione L, Caron J-F, Godonou P, van IJselmuijden K, Knippers J, Mottram T, et al. Prospect for new guidance in the design of FRP: Support to the implementation, harmonization and further development of the Eurocodes: Publications Office of the European Union, 2016.

[17] Liu T, Harries KA. Flange local buckling of pultruded GFRP box beams. Compos Struct 2018;189:463–72.

[18] Baran I. Pultrusion: state-of-the-art process models. Smithers Rapra 2015.

[19] Ramôa Correia J. 9 - Pultrusion of advanced fibre-reinforced polymer (FRP) composites. In: Bai J, editor. Advanced Fibre-Reinforced Polymer (FRP) Composites for Structural Applications: Woodhead Publishing; 2013. p. 207-51.

[20] Alajarmeh O, Zeng X, Aravinthan T, Shelley T, Alhawamdeh M, Mohammed A, et al. Compressive behaviour of hollow box pultruded FRP columns with continuous-wound fibres. Thin-Walled Struct 2021;168:108300.

[21] Alhawamdeh M, Alajarmeh O, Aravinthan T, Shelley T, Schubel P, Mohammed A, et al. Review on Local Buckling of Hollow Box FRP Profiles in Civil Structural Applications. Polymers (Basel) 2021;13.

[22] Alhawamdeh M, Alajarmeh O, Aravinthan T, Shelley T, Schubel P, Kemp M, et al. Modelling hollow pultruded FRP profiles under axial compression: Local buckling and progressive failure. Compos Struct 2021;262.

[23] Lightfoot JS, Wisnom MR, Potter K. A new mechanism for the formation of ply wrinkles due to shear between plies. composites Part A. Applied Science and Manufacturing 2013;49:139–47.

[24] Roy SS, Zou W, Potluri P. Influence of braid carrier tension on carbon fibre braided preforms. In: Kyosev Y, editor. Recent Developments in Braiding and Narrow Weaving. Cham: Springer International Publishing; 2016. p. 91–102.

[25] Kyosev Y. Advances in braiding technology: Specialized techniques and applications. Woodhead Publishing; 2016.

[26] Wang Y, Gu Y, Liu J. A domain-decomposition generalized finite difference method for stress analysis in three-dimensional composite materials. Appl Math Lett 2020; 104:106226.

[27] Kabir H, Aghdam MM. A robust Bézier based solution for nonlinear vibration and post-buckling of random checkerboard graphene nano-platelets reinforced composite beams. Compos Struct 2019;212:184–98.

[28] Bert CW, Malik M. Differential quadrature: a powerful new technique for analysis of composite structures. Compos Struct 1997;39:179–89.

[29] GB/T 31539. Pultruded fiber reinforced polymer composites structural profiles. Standardization Administration of China. 2015 [in Chinese].

[30] Zhang L, Zhang S, Xu D, Chen X. Compressive behavior of unidirectional FRP with spacial fibre waviness and non-uniform fibre packing. Compos Struct 2019;224: 111082.

[31] Feng H, Wu Y, Liu T. Non-uniform fiber-resin distributions of pultruded GFRP profiles. Composites Part B: Engineering; 2021.

[32] Wilhelmsson D, Gutkin R, Edgren F, Asp LE. An experimental study of fibre waviness and its effects on compressive properties of unidirectional NCF composites. Compos A Appl Sci Manuf 2018;107:665–74.

[33] Qi S, Alajarmeh O, Shelley T, Schubel P, Rendle-Short K, Zeng X. Fibre waviness characterisation and modelling by Filtered Canny Misalignment Analysis (FCMA). Compos Struct 2023;307:116666.

[34] Poulton M, Sebastian W. Taxonomy of fibre mat misalignments in pultruded GFRP bridge decks. Compos A Appl Sci Manuf 2021:142.

[35] Baran I, Straumit I, Shishkina O, Lomov SV. X-ray computed tomography characterization of manufacturing induced defects in a glass/polyester pultruded profile. Compos Struct 2018;195:74–82.

[36] Netzel C, Mordasini A, Schubert J, Allen T, Battley M, Hickey CMD, et al. An experimental study of defect evolution in corners by autoclave processing of prepreg material. Compos A Appl Sci Manuf 2021:144.

[37] Qi S, Alajarmeh O, Shelley T, Schubel P, Rendle-Short K, Zeng X. Formation of non-uniform fibre distributions in winding-pultrusion process and its effect on axial compressive properties of hollow GFRP profiles. Compos A Appl Sci Manuf 2023; 173:107659.

[38] ASTMD7249/D7249M. Standard test method for facing properties of sandwich constructions by long beam flexure. Am Soc Test Mater. 2012.

[39] Kollar LP, Springer GS. Mechanics of composite structures. Cambridge University Press; 2003.

[40] Feo L, Mosallam AS, Penna R. Mechanical behavior of web–flange junctions of thin-walled pultruded I-profiles: An experimental and numerical evaluation. Compos B Eng 2013;48:18–39.

[41] Huang Z, Li D, Uy B, Thai H-T, Hou C. Local and post-local buckling of fabricated high-strength steel and composite columns. J Constr Steel Res 2019;154:235–49.

[42] Al-saadi AU, Aravinthan T, Lokuge W. Effects of fibre orientation and layup on the mechanical properties of the pultruded glass fibre reinforced polymer tubes. Eng Struct 2019;198.

[43] Alhawamdeh M, Alajarmeh O, Aravinthan T, Shelley T, Schubel P, Mohammad A, et al. Modelling flexural performance of hollow pultruded FRP profiles. Compos Struct 2021;276.

[44] Barbero EJ. Introduction to composite materials design. CRC Press; 2010.

[45] Almeida-Fernandes L, Silvestre N, Correia JRJCPBE. Characterization of transverse fracture properties of pultruded GFRP material in tension. 2019;175:107095.

[46] Alhawamdeh M, Alajarmeh O, Aravinthan T, Shelley T, Schubel P, Mohammed A, et al. Design optimisation of hollow box pultruded FRP profiles using mixed integer constrained Genetic algorithm. Compos Struct 2022;302:116247.

[47] Alajarmeh O, Alhawamdeh M, Shelley T, Mohammed A, Nicol L, Schubel P, et al. Influence of post-processing on the compressive behaviour of full-scale pultruded FRP columns: Holes and inserts. Eng Struct 2022;266:114547.

[48] Van Paepegem W, De Geyter K, Vanhooymissen P, Degrieck J. Effect of friction on the hysteresis loops from three-point bending fatigue tests of fibre-reinforced composites. Compos Struct 2006;72:212–7.

[49] Huang W, Causse P, Hu H, Belouettar S, Trochu F. Transverse compaction of 2D glass woven fabrics based on material twins - Part I: Geometric analysis. Compos Struct 2020;237:10.

[50] Qiao P, Shan L. Explicit local buckling analysis and design of fiber–reinforced plastic composite structural shapes. Compos Struct 2005;70:468–83.

[51] Ascione L, Caron J-F, Godonou P, van IJselmuijden K, Knippers J, Mottram T, et al. Prospect for new guidance in the design of FRP. Ispra: EC Joint Research Centre. 2016.